Ice shelf basal melt rates in the Amundsen Sea at the end of the 21st century

Nicolas C. Jourdain[1], Pierre Mathiot[1], Clara Burgard [1], Justine Caillet[1], Christoph Kittel[1]

[1]Univ. Grenoble Alpes/CNRS/IRD/G-INP, Institut des Géosciences et de l'Environnement, Grenoble, France

Key Points:

- We present 1/12° ocean–sea-ice–ice-shelf projections at the end of the 21st century under the RCP8.5 scenario.
- Ice shelf melt rates in the Amundsen Sea are typically multiplied by 1.4 to 2.2 from 1989–2009 to 2080–2100.
- Advection of warmer water from remote locations and reduced Ekman downwelling are the main drivers of changes in ice shelf melt rates.

Corresponding author: Nicolas C. Jourdain, nicolas.jourdain@univ-grenoble-alpes.fr

Abstract

Antarctic Ice Sheet projections show the highest sensitivity to increased basal melting in the Amundsen Sea sector. However, little is known about the melt rates that could be reached in 2100 in this region. We build an ensemble of three ocean–sea-ice–ice-shelf simulations for both the recent decades and the late 21st century. Our projections are constrained by regional atmosphere simulations and the multi-model mean climate change of the 5th Climate Model Intercomparison Project under the RCP8.5 scenario. The ice shelf melt rates are typically multiplied by 1.4 to 2.2 from present day to future, for a total basal mass loss increased by 347 Gt yr^{-1}. This is approximately equally explained by advection of warmer water from remote locations and by regional changes in Ekman downwelling and in the ice-shelf melt-induced circulation. Our simulations suggest that high-end melt projections previously used to constrain recent sea level projections may have been significantly overestimated.

Plain Language Summary

Future sea level rise highly depends on how fast the ocean will melt the floating ice shelves in Antarctica, which modulates the ice flow from the ice sheet into the ocean. This is particularly true for the Amundsen Sea sector where the ice flow into the ocean is very sensitive to ocean-induced melting. Here we use a numerical model that represents the evolution of the Amundsen Sea, including under the floating ice shelves. Under a high-end greenhouse-gases concentration pathway, our simulations indicate that melt rates beneath the ice shelves may increase by 40 to 120%. This is explained by both warmer seawater coming from distant regions and changes in the local wind stress. Our simulations suggest that high-end melt projections previously used to constrain recent sea level projections may have been overestimated.

1 Introduction

Most projections of the Antarctic contribution to sea level rise are based on standalone ice sheet models in which melting beneath ice shelves is parameterized (Levermann et al., 2020; Seroussi et al., 2020; DeConto et al., 2021; Edwards et al., 2021). The existing melt parameterizations are based on highly simplified representations of the ocean circulation and heat exchanges in ice shelf cavities, and the resulting melt rates are significantly biased (Favier et al., 2019; Burgard et al., 2022). Furthermore, these melt parameterizations are typically driven by ocean warming derived from simulations of the Climate Model Intercomparison Project (CMIP, Eyring et al., 2016), although ice shelf cavities are not represented and ocean properties on the Antarctic continental shelf are significantly biased (Purich & England, 2021).

To either trust or challenge these ice sheet and sea level projections, our community needs projections that resolve the ocean dynamics over the Antarctic continental shelf and beneath the ice shelves, but such projections are rare (Asay-Davis et al., 2017). Timmermann and Hellmer (2013) and Naughten et al. (2018) pioneered CMIP-based projections at the Antarctic scale, using a global ocean model with refined resolution around Antarctica and beneath ice shelves. Their projections were nonetheless of limited use for the Amundsen Sea sector because of a substantial cold bias in their present-day state. Siahaan et al. (2021) were the first to run a global climate model (i.e., land, ocean, atmosphere) with an interactive Antarctic Ice Sheet in scenario-based projections. Their present-day melt rates were reasonable in the Amundsen Sea, but they found little change in their projections and questioned the representation of the Amundsen cavities at their resolution (e.g., only 11 grid columns for Pine Island ice shelf cavity). Stronger present-day biases were nonetheless found at higher ocean resolution in their model configuration (Smith et al., 2021).

Given that the Antarctic Ice Sheet projections show the highest sensitivity to increased basal melting in the Amundsen Sea sector (together with the Wilkes Land sector, Seroussi et al., 2020), it seems crucial to better estimate possible future ice shelf melt rates in that region and describe the associated mechanisms. Recent simulations of the Amundsen Sea by Naughten et al. (2022) have shown that relatively warm periods become more dominant over the 20$^{\text{th}}$ century, causing stronger ice shelf melting. In this paper, we use a regional ocean–sea-ice–ice-shelf model to build new projections to 2100 under the RCP8.5 scenario for the Amundsen Sea region and to describe the mechanisms explaining changes in ice shelf melt rates. Then, we use these ocean projections to assess existing melt parameterizations recently used in ice sheet projections.

2 Ocean–sea-ice–ice-shelf simulations

We make use of the NEMO-3.6 (Nucleus for European Modelling of the Ocean, Madec & NEMO-team, 2016) ocean model that includes the LIM3 (Louvain Ice Model, Rousset et al., 2015) sea ice model and the ice shelf cavity module developed by Mathiot et al. (2017). The grid extends from 142.1°W to 84.9°W and from 76.5°S to 59.7°S, and has a resolution of 1/12° in longitude, i.e., a quasi-isotropic resolution varying from 4.7 km at the northern boundary to 2.2 km in the southernmost part of the domain. We use 75 vertical levels of thickness ranging from 1 m at the surface to 204 m at 6000 m depth.

To get a rough estimate of the model uncertainty, we run an ensemble of three present-day and future simulations. For ensemble member A, the ice shelf and seabed topography is extracted from BedMachine-Antarctica-v1.33 (Morlighem et al., 2020), while members B and C are based on BedMachine-Antarctica-v2.0 (Morlighem, 2020). Additionally, B and C include a representation of grounded tabular icebergs, in particular B22A (Antarctic Iceberg Tracking Database, Budge & Long, 2018), whose ungrounded parts are treated as an ice shelf, and the line of icebergs grounded on Bear Ridge (Nakayama et al., 2014; Bett et al., 2020). The heat exchange coefficient (Γ_T) is 2.21×10^{-2} in A vs 1.88×10^{-2} in B-C, while the salt exchange coefficient is always defined as $\Gamma_S = \Gamma_T/35$. Finally, two parameters of the sea ice model differ: the maximum permitted sea ice concentration is set to 99.9% of the mesh in A-B vs 95% in C, and the ice–ocean drag coefficient is set to 5.0×10^{-3} in A-B vs 2.5×10^{-3} in C. All these parameter values are commonly used in the NEMO community. Our ensemble is designed to simply illustrate the importance of a few empirical choices and cannot be considered as a deep exploration of NEMO's parametric uncertainty (e.g., Williamson et al., 2017).

Our present-day simulations cover 1989–2009, following 10 years of spin up from 1979. The surface boundary conditions consist of 3-hourly (temperature, humidity, wind velocity) and daily (radiative fluxes and precipitation) mean outputs of the 10 km MAR (Regional Atmospheric Model, Gallée & Schayes, 1994) configuration described and evaluated by Donat-Magnin et al. (2020). The lateral ocean and sea ice boundary conditions consist of 5-day mean outputs of a global 0.25° NEMO simulation very similar to the one described by Merino et al. (2018) except that it is spun up from 1958 and that the imposed ice shelf melt flux increases linearly from 1990 to 2005 and is constant before and after that, with values corresponding to the FRESH+ and FRESH− reconstructions of Merino et al. (2018). The global 0.25° simulation represents Lagrangian icebergs (Merino et al., 2016), and their 5-day averaged melt rate (Jourdain et al., n.d.) is applied at the surface of our regional 1/12° configuration. Our present-day simulations are evaluated in sup. section S1. Inn summary, our simulations are too warm at depth by approximately 0.5°C, and ice shelf melt rates are consequently slightly overestimated.

Our future simulations cover 2080–2100 in addition to 10 years of spin up from the same initial state as our present-day simulation, i.e., 1979. Our projections are representative of the CMIP5 multi-model mean under the RCP8.5 concentration pathway. The surface boundary conditions are taken from the MAR regional projections described and

evaluated through a perfect-model approach in Donat-Magnin et al. (2021). The atmospheric projections themselves were driven at their surface and lateral boundaries by the mean seasonal anomalies (2080–2100 minus 1989–2009) derived from 33 CMIP5 models under the RCP8.5 scenario (more details are provided in Donat-Magnin et al., 2021).

The applied anomalies induce an eastward zonal wind and sea ice stress anomaly along the shelf break and offshore (Fig. 1a,b), which is a known response of the CMIP models to high greenhouse gases concentrations by 2100 (Swart & Fyfe, 2012; Holland et al., 2019; Goyal et al., 2021). We also find an increased westward stress along most of the ice sheet margin (Fig. 1b), which is possibly related to higher air temperature gradient across the ice-sheet–ocean boundary in the presence of reduced sea ice cover in the future. On average over the continental shelf, the Ekman downward velocity due to the wind and sea ice stress is weakened by 50% in the future compared to present day (sup. section S2).

In terms of surface heat fluxes, the Amundsen continental shelf loses 41% less energy to the atmosphere in the future compared to present-day (Fig. 1c,d), which is consistent with the effect of a warmer troposphere on downward sensible and longwave heat fluxes over the open ocean and sea ice. Precipitation increases by 22% (Fig. 1e,f) due to a higher water holding capacity of the troposphere in a warmer climate (Donat-Magnin et al., 2021). The increased precipitation and the reduced sea ice production over the continental shelf (from 0.23 to 0.19 $\mathrm{Gt\,yr^{-1}}$) are together responsible for an annual rate of surface buoyancy loss reduced by 75% in the future compared to present day (supp. section S2).

We adopt a similar approach for the lateral boundaries of our regional ocean–sea-ice simulations and add the CMIP5 multi-model mean seasonal anomalies to the present-day lateral boundary conditions (for temperature, salinity, ocean velocity, sea ice concentration, sea ice thickness, and snow-on-ice thickness). The perturbation applied at our lateral boundaries is comprehensively described in sup. section S3, which can be summarised as a warming that exceeds 0.25°C everywhere in the first 1000 m and reaches 2°C in the northernmost part of our domain, as well as a freshening of the first 100 m that is particularly pronounced near the Antarctic coast.

Two additional sensitivity experiments are performed for further insight into the processes. First, we repeat the future simulation of ensemble member B but we only apply the future surface forcing, i.e., we keep the present-day lateral boundary conditions for ocean and sea ice. Second, we repeat the future simulation of ensemble member C but with increased iceberg melting (which is kept at present-day values in the other experiments). Following the calculations presented in section S4, we increase the total iceberg melt flux over the Amundsen continental shelf from 63 $\mathrm{Gt\,yr}-1$ at present-day to 136 $\mathrm{Gt\,yr^{-1}}$ at the end of the 21st century under RCP8.5 (Fig. 1g,h).

3 Results: changes in ice shelf basal melting and related processes

On average over the three ensemble members, the ice shelf melt rates are multiplied by 1.4 to 2.2 (depending on the ice shelf) from present day to future (Fig. 2a). The total ice shelf meltwater flux in the Amundsen Sea increases by 347 $\mathrm{Gt\,yr^{-1}}$ on average (Fig. 2b,c), with a standard deviation of 54 $\mathrm{Gt\,yr^{-1}}$ across the ensemble. This is much larger than the 73 $\mathrm{Gt\,yr^{-1}}$ of increased iceberg melting (Fig. 1h), 40 $\mathrm{Gt\,yr^{-1}}$ of increased precipitation (Fig. 1f), and a sea ice production decreased by 37 $\mathrm{Gt\,yr^{-1}}$ which is equivalent to a freshwater release of 30 $\mathrm{Gt\,yr^{-1}}$ (for a sea ice salinity of 6.3 $\mathrm{g\,kg^{-1}}$). Even though a part of the ice shelf meltwater is mixed at depth and does not reach the surface layer, the additional ice shelf melt seems to be the major driver of increased buoyancy in the surface layer.

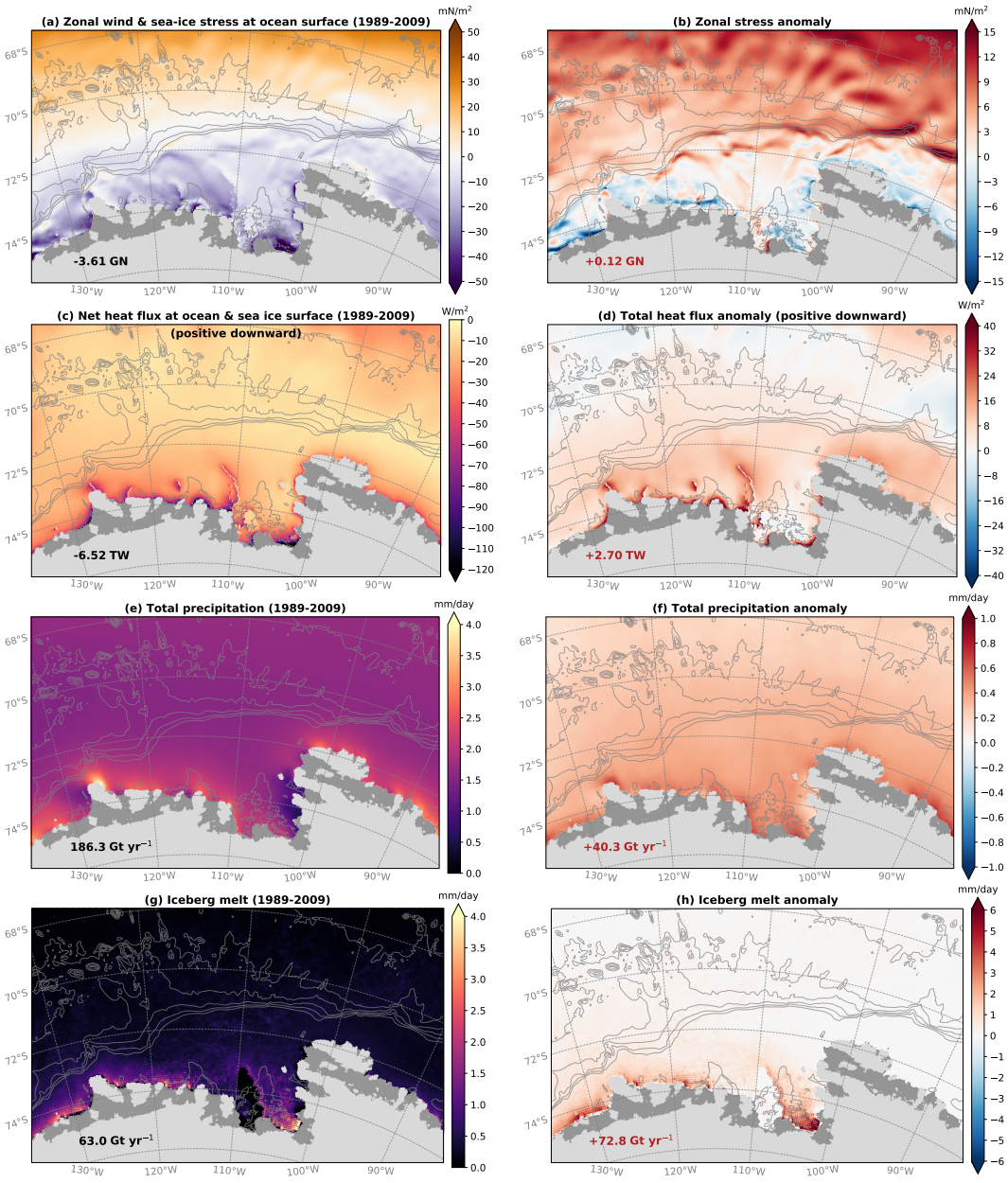

Figure 1. Present-day atmospheric forcing (left) and future anomalies with respect to present day (right). Anomalies are calculated as the average of 2080–2100 minus 1989–2009. The grounded ice sheet and the ice shelves are shaded in light and dark grey, respectively. The grey contours indicate the bathymetry (every 750 m). Numbers near the lower left corner indicate the value of the plotted field integrated over the continental shelf, which is defined as the area between the 1500 m isobath and the coastline, and between 100°W and 135°W.

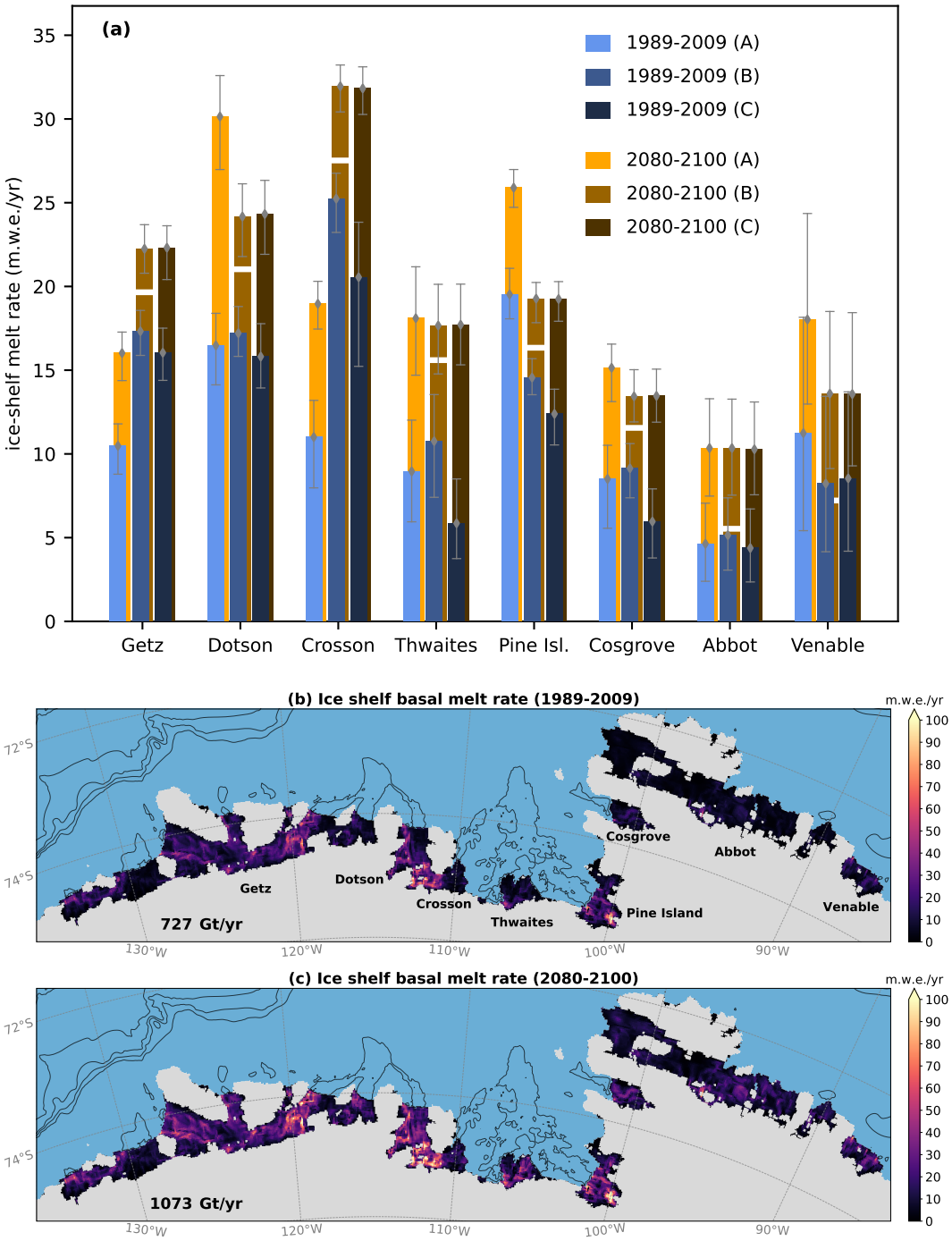

Figure 2. (a) Mean present day and future melt rates of individual ice shelves in model configurations A, B and C (in meters of liquid water equivalent per year, i.e. 10^3 kg m^{-2} yr^{-1}). The grey bars cover 95% of the monthly values, i.e. between the 2.5$^{\text{th}}$ and the 97.5$^{\text{th}}$ percentiles. The white disruption of the light brown bars (B over 2080-2100) represent the future melt rate in the experiment with lateral boundary conditions kept at present-day values. (b,c) Present-day and future ice shelf melt rates, and integrated value over the domain in the lower left corner. The black contours indicate the bathymetry (every 750 m).

Interestingly, members B and C give almost identical future melt rates while present-day values differ significantly (Fig. 2a). As the only difference between B and C is the set of sea ice parameters, this indicates that sea ice production and the related surface buoyancy flux are important drivers of ice shelf melting presently, but no longer play a role in the future. This is very likely related to both the 75% reduction of the surface buoyancy loss in the future and the mixing of more ice shelf meltwater into the surface layer. Both increase the ocean stratification and prevent surface waters from reaching deeper warmer layers on the continental shelf through convective mixing. We also do not find any significant difference between projection C with and without increased iceberg melt rates (not shown), which supports the idea of a decoupling between the surface and the deeper layers in the future.

The changes in melt rates for member B without perturbations of NEMO's lateral boundaries are shown by the white disruption of the middle brown bars in Fig. 2a. Increased melt rates underneath Abbot and Venable ice shelves are almost entirely explained by the modified lateral boundary conditions. For the other ice shelves, the part of increased melt rate attributed to the lateral boundaries varies from 1/3 to 2/3 of the total change, depending on the ice shelf. This indicates that future changes in remote ocean properties are important, i.e., local changes in the atmospheric forcing cannot entirely explain the projected increase in ice shelf melt rates.

We then use the terms of the exact heat and salt budget (saved online and calculated as in Jourdain et al., 2017) to get further insights into the physical mechanisms. The offshore projection is characterised by a 0.25°C warming below the thermocline due to horizontal advection from the domain boundaries, a 75 m higher thermocline explained by horizontal advection and decreased convective mixing due to less sea ice formation, and a surface freshened by 0.4 $\mathrm{g\,kg^{-1}}$ (more details are provided in sup. section S4). Changes over the continental shelf are more intense, with 0.5°C warming at depth, a 160 m higher thermocline (Fig. 3a), and surface freshened by 0.5 $\mathrm{g\,kg^{-1}}$ (Fig. 3b). In contrast to the offshore mechanisms, vertical advection plays a key role on the continental shelf (Fig. 3c,d). Approximately half of the heat brought by changes in vertical advection between 250 and 800 m is due to the melt-induced circulation in ice shelf cavities and is mostly consumed as latent heat for ice melting (compare Fig. 3c,d to Fig. 3e,f). The remaining part is consistent with the reduced Ekman downwelling described in the previous section and in Spence et al. (2014) and Naughten et al. (2022), which reduces the downward advection of relatively cold and fresh water from the surface layer (above 250 m) to deeper layers (Fig. 3c,d). A closer look at the budget terms within ice shelf cavities (not shown) reveals an additional input of heat and freshwater between 100 and 400 m depth corresponding to the melt-induced circulation that releases a mixture of meltwater and entrained CDW at the ice shelf front as described by Jourdain et al. (2017).

4 Results: assessment of simple ice shelf melt parameterizations

Here we use our NEMO projections to assess the non-local (also referred to as semi-local) quadratic parameterization proposed by Favier et al. (2019) and used in some of the standard ice sheet projections of the Ice Sheet Model Intercomparisaon Project for CMIP6 (ISMIP6, Nowicki et al., 2020; Seroussi et al., 2020), with a melt rate defined as:

$$m(x,y) = K \times (TF(x,y,z_{\mathrm{draft}}) + \delta T) \times |\langle TF \rangle_{\mathrm{ice\text{-}shelf}} + \delta T| \quad (1)$$

where $TF(x,y,z_{\mathrm{draft}})$ is the thermal forcing at the ice-ocean interface of depth z_{draft}, and $\langle TF \rangle_{\mathrm{ice\text{-}shelf}}$ the thermal forcing averaged over an entire ice shelf draft. The temperature correction δT is used to correct biases in present-day observations and to account for melt-induced cooling or other poorly represented processes (Jourdain et al., 2020). K is a tuning coefficient that was expressed in various ways across previous studies. An expression of K was proposed by Favier et al. (2019) and Jourdain et al. (2020), including a γ_0 tuning parameter, but we find that the expression proposed by Jenkins et al. (2018) and Burgard

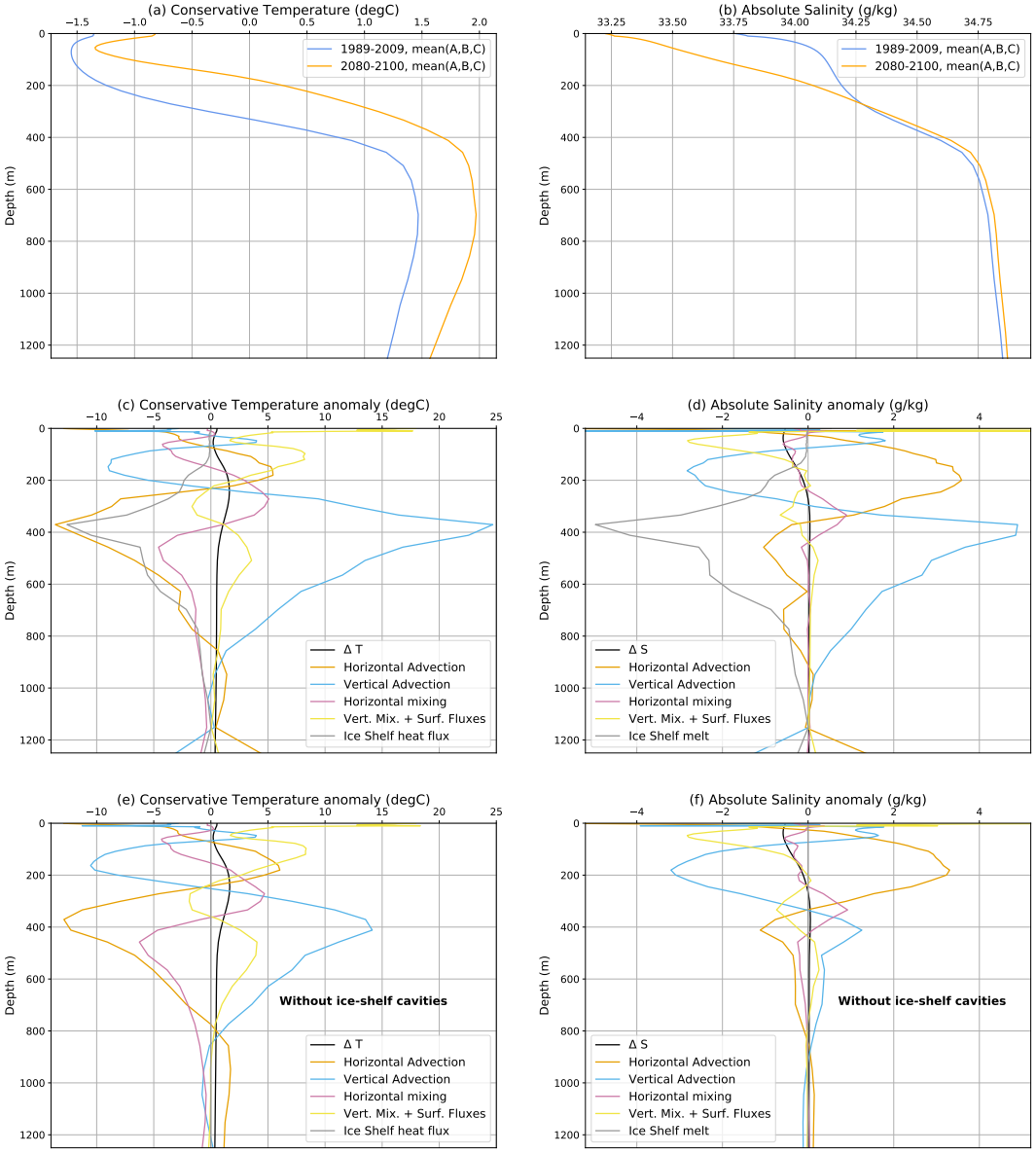

Figure 3. (a,b) Present-day and future conservative temperature and absolute salinity profiles over the Amundsen Sea continental shelf (defined as the area between the 1500 m isobath and the coastline, and between 100°W and 135°W), including ice shelf cavities. (c,d) temperature (ΔT) and salinity (ΔS) change from present-day to future conditions and contributions of the individual terms of the heat and salt equations to ΔT and ΔS, respectively. (e,f) same as (c,d) but excluding ice shelf cavities.

et al. (2022) more physically sound, which is why we keep a general formulation for K. For ISMIP6, Jourdain et al. (2020) proposed two calibration methods, one referred to as "MeanAnt", ensuring realistic present-day melt rates at the scale of Antarctica for minimal temperature corrections and giving $K_{\mathrm{MeanAnt}} = 2.57\ \mathrm{m\,yr^{-1}\,K^{-2}}$, and the other one referred to as "PIGL", ensuring realistic present-day melt rates near Pine Island's grounding line and giving $K_{\mathrm{PIGL}} = 28.2\ \mathrm{m\,yr^{-1}\,K^{-2}}$, but requiring negative δT corrections almost everywhere to keep reasonable melt rates for individual ice shelves or integrated over larger sectors.

In the following, we assume that the present-day temperature is perfectly known, so that we can use $\delta T = 0$ for MeanAnt and we find that present-day RMSE from PIGL are lowest for $\delta T = -1.9$°C. For clarity, we just show the results for Pine Island and Thwaites (Fig. 4), which are key ice shelves for the Antarctic contribution to sea level rise, but the other ice shelves have a very similar behaviour. We estimate the future parameterized melt rates in two ways: (1) from the future ocean temperatures simulated by NEMO (orange dashed curves in Fig. 4), and (2) from the CMIP5 multi-model mean ocean warming added to the NEMO present-day temperatures (dashed dark red curves in Fig. 4) which corresponds to what is commonly used in standalone ice sheet projections like ISMIP6.

First of all, the present-day melt rates have overall a realistic magnitude although the exact vertical distribution is only poorly captured (blue curves in Fig. 4). The MeanAnt curves show some overlap between the three model projections and the 90$^{\mathrm{th}}$ confidence interval of the parameterized projections (orange curves in Fig. 4a,b), although the RMSE approximately doubles compared to present day. The PIGL projections are much worse, with very little overlap between the three model projections and the 90$^{\mathrm{th}}$ confidence interval of the parameterized projections (orange curves in Fig. 4c,d). For the 95$^{\mathrm{th}}$ percentile of K, the maximum melt rates in either Pine Island or Thwaites cavity are overestimated by a factor of five. The melt projections directly based on the CMIP5 ocean warming (dashed dark red curves in Fig. 4) are similar to the projections from the warming produced by NEMO, indicating that most of the bias comes from the parameterization itself.

5 Discussion and conclusion

In this paper, we have built an ensemble of three 1/12° ocean–sea-ice–ice-shelf projections of the late 21$^{\mathrm{st}}$ century under the RCP8.5 concentration pathway. In these simulations, the net surface buoyancy loss is reduced by 75% in the future compared to present day due to surface freshening by increased precipitation, increased iceberg melt and reduced sea ice production. Increased ice shelf melt also largely contributes to making the surface layer fresher and more buoyant in the future. The result is a decoupling between the surface layer and deeper layers on the continental shelf, which makes future ice shelf melt insensitive to additional perturbations of surface buoyancy fluxes. We find that the future Ekman downwelling velocity is reduced by half over the continental shelf compared to present day. This, in addition to the melt-induced circulation, largely explains the additional heat made available to ice shelf melting. However, regional changes in atmospheric forcing only explain 1/3 to 2/3 of the increase in ice shelf melt rates (depending on the ice shelf). The remaining is due to advection of warmer water from remote locations (i.e. from our model domain lateral boundaries). The importance of advection from remote locations was already evidenced by Nakayama et al. (2018) for the interannual variability of the Amundsen Sea. Here we clearly show the caveats of projecting future ice shelf melting in the Amundsen Sea simply based on regional atmospheric perturbations (as done in previous studies, such as Holland et al., 2019; Naughten et al., 2022). The relative changes in melt rates are lower than previous estimates (Timmermann & Hellmer, 2013; Naughten et al., 2018), but higher in absolute value, which we believe is more realistic as we start from more realistic present-day conditions.

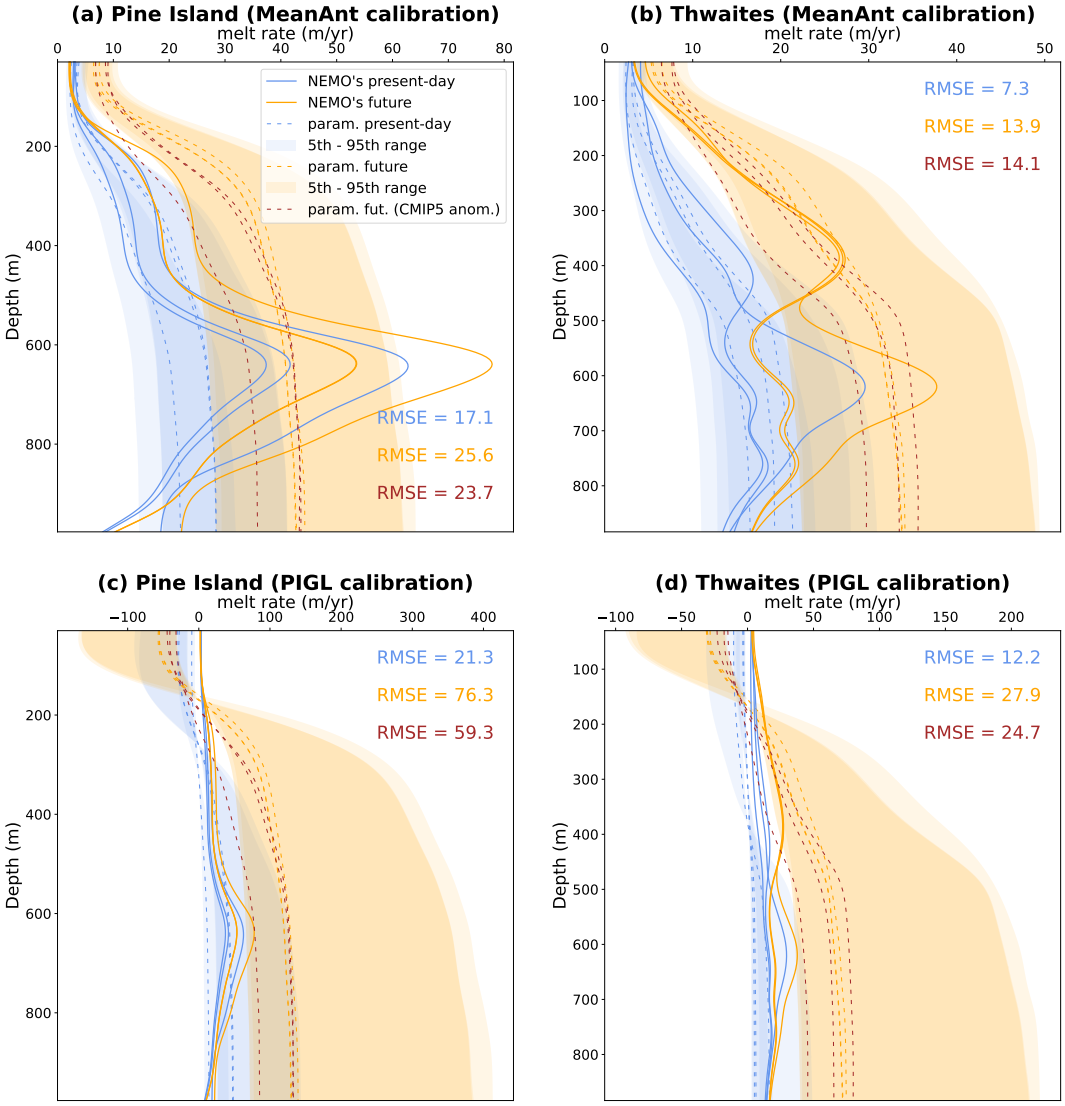

Figure 4. Melt profiles beneath Pine Island (left) and Thwaites (right) ice shelves, from the NEMO simulations (solid lines), and from the ISMIP6 standard parameterization (dashed lines) tuned following either the "MeanAnt" (upper panels) or the "PIGL" (lower panels) method (median K coefficient derived from Jourdain et al., 2020). The present day parameterized melt rates are based on NEMO's present-day temperatures in front of the ice shelf cavities (within 50 km from the ice shelf front). The future melt rate is either calculated from the's future temperatures simulated by NEMO (orange dashed lines) or from the CMIP5 multi-model mean temperature anomaly (dark red dashed lines). The semi-transparent shaded areas indicate the range corresponding to the 5^{th} and 95^{th} percentiles of K coefficients based on the future temperatures produced by NEMO (values derived from Tab. 2 of Jourdain et al. 2020). The three curves for each estimate correspond to the three members of our small ensemble. Every curve is built using a kernel density estimate based on a Gaussian function of standard deviation equal to $1/20^{\text{th}}$ of the maximum ice draft depth. The Root Mean Square Errors (RMSE, in m/yr) are calculated for the spatial pattern with regards to the NEMO values and correspond to the median K values.

All our conclusions are nonetheless based on a single ocean model, even if we used three different set-ups, and it will be important to challenge these results using completely different ocean models and different projection methods. An important limitation of our study is that there is no ice sheet model coupled to NEMO, i.e., ice shelves are static. This was shown to be an important limitation donat-magnin17, albeit for much stronger and longer melt perturbations. In terms of projection method, we have chosen to drive our projections directly by the CMIP multi-model mean because it is often considered as the best estimate for future climate as individual model biases are partly cancelled (Knutti et al., 2010). The use of future anomalies with respect to present day is expected to remove a part of the biases in individual model projections given that the CMIP model biases are largely stationary even under strong climate changes (Krinner & Flanner, 2018), while conserving linearities like the geostrophic balance. However, an important limitation of our projection method is that we do not account for possible changes in the frequency of interannual events like El Niño (Cai et al., 2014), and it will be important to confront our results to direct downscaling of the CMIP models. Finally, we have chosen to force our ocean simulations using a 10 km regional atmospheric model, which is expected to be more realistic along the coastline and the shelf break than the much coarser CMIP models (e.g., Dinniman et al., 2015; Huot et al., 2021), although the use of such an intermediate model may be an additional source of biases and uncertainty in the chain of projections.

Finally, given that the Antarctic Ice Sheet projections show the highest sensitivity to increased basal melt rates in the Amundsen Sea sector seroussi20, our regional results can provide a critical perspective on the Antarctic contribution to the 21st century sea level rise simulated within ISMIP6 (Seroussi et al., 2020) and emulated by Edwards et al. (2021). The high-end estimates for 2100 under RCP8.5 ($\sim$30 cm of additional sea level) were obtained from the 95th percentile of the PIGL parameters, which we find highly incompatible with our simulations. Edwards et al. (2021) empirically defined a continuous distribution of K coefficients (their Fig. 3d), with a relatively large cumulative probability around the median PIGL parameter, and low-probability extreme values beyond the 95th percentile of PIGL parameters. Our projections suggest that this distribution should be narrowed towards lower values and that lower parameters should be used even for risk averse projections.

Data and softwares

The model version and set of parameters used to run our experiments are provided in `http://github.com/nicojourdain/NEMO_PARAMS_SIMU`. All the python scripts used to build the figures are provided in `http://github.com/nicojourdain/SCRIPTS_PAPER_PLOTS` and are mainly based on the Xarray (Hoyer & Hamman, 2017), Numpy (Harris et al., 2020) and Matplotlib (Hunter, 2007) packages. THE GITHUB REPOSITORIES WILL BE ARCHIVED ON `http://zenodo.org` AFTER ACCEPTANCE.

Acknowledgments

This publication is PROTECT contribution number XX. This study was funded by the European Union's Horizon 2020 research and innovation programme under grant agreements No 869304 (PROTECT), No 820575 (TiPACCs) and No 101003826 (CRiceS). It was also partly funded by the French National Research Agency under grant No ANR-19-CE01-0015 (EIS). This work was granted access to the HPC resources of CINES under the allocation A0100106035 attributed by GENCI.

References

Asay-Davis, X. S., Jourdain, N. C., & Nakayama, Y. (2017). Developments in Sim-

ulating and Parameterizing Interactions Between the Southern Ocean and the Antarctic Ice Sheet. *Current Climate Change Reports*, *3*(4), 316–329.

Bett, D. T., Holland, P. R., Naveira Garabato, A. C., Jenkins, A., Dutrieux, P., Kimura, S., & Fleming, A. (2020). The impact of the Amundsen Sea freshwater balance on ocean melting of the West Antarctic Ice Sheet. *J. Geophys. Res. Oceans*, *125*(9), e2020JC016305.

Budge, J. S., & Long, D. G. (2018). A comprehensive database for Antarctic iceberg tracking using scatterometer data. *IEEE Journal of Selected Topics in Applied Earth Observations and Remote Sensing*, *11*(2), 434–442.

Burgard, C., Jourdain, N. C., Reese, R., Jenkins, A., & Mathiot, P. (2022). An assessment of basal melt parameterisations for Antarctic ice shelves. *The Cryosphere Discussion*, *0*, 0–0.

Cai, W., Borlace, S., Lengaigne, M., Van Rensch, P., Collins, M., Vecchi, G., ... others (2014). Increasing frequency of extreme El Niño events due to greenhouse warming. *Nat. Clim. Change*, *4*(2), 111–116.

DeConto, R. M., Pollard, D., Alley, R. B., Velicogna, I., Gasson, E., Gomez, N., ... others (2021). The Paris Climate Agreement and future sea-level rise from Antarctica. *Nature*, *593*(7857), 83–89.

Dinniman, M. S., Klinck, J. M., Bai, L.-S., Bromwich, D. H., Hines, K. M., & Holland, D. M. (2015). The Effect of Atmospheric Forcing Resolution on Delivery of Ocean Heat to the Antarctic Floating Ice Shelves. *J. Climate*, *28*(15), 6067–6085.

Donat-Magnin, M., Jourdain, N. C., Gallée, H., Amory, C., Kittel, C., Fettweis, X., ... Agosta, C. (2020). Interannual Variability of Summer Surface Mass Balance and Surface Melting in the Amundsen Sector, West Antarctica. *The Cryosphere*, *14*(1), 229–249.

Donat-Magnin, M., Jourdain, N. C., Kittel, C., Agosta, C., Amory, C., Gallée, H., ... Chekki, M. (2021). Future surface mass balance and surface melt in the Amundsen sector of the West Antarctic Ice Sheet. *The Cryosphere*, *15*(2), 571–593.

Edwards, T. L., Nowicki, S., Marzeion, B., Hock, R., Goelzer, H., Seroussi, H., ... others (2021). Projected land ice contributions to twenty-first-century sea level rise. *Nature*, *593*(7857), 74–82.

Eyring, V., Bony, S., Meehl, G. A., Senior, C. A., Stevens, B., Stouffer, R. J., & Taylor, K. E. (2016). Overview of the Coupled Model Intercomparison Project Phase 6 (CMIP6) experimental design and organization. *Geosci. Model Dev.*, *9*(5), 1937–1958.

Favier, L., Jourdain, N. C., Jenkins, A., Merino, N., Durand, G., Gagliardini, O., ... Mathiot, P. (2019). Assessment of Sub-Shelf Melting Parameterisations Using the Ocean-Ice Sheet Coupled Model NEMO (v3. 6)-Elmer/Ice (v8. 3). *Geosci. Model Dev.*.

Gallée, H., & Schayes, G. (1994). Development of a three-dimensional meso-γ primitive equation model: katabatic winds simulation in the area of Terra Nova Bay, Antarctica. *Monthly Wea. Rev.*, *122*(4), 671–685.

Goyal, R., Sen Gupta, A., Jucker, M., & England, M. H. (2021). Historical and projected changes in the southern hemisphere surface westerlies. *Geophys. Res. Lett.*, *48*(4), e2020GL090849.

Harris, C. R., Millman, K. J., van der Walt, S. J., Gommers, R., Virtanen, P., Cournapeau, D., ... others (2020). Array programming with NumPy. *Nature*, *585*(7825), 357–362. Retrieved from `https://doi.org/10.1038/s41586-020-2649-2` doi: 10.1038/s41586-020-2649-2

Holland, P. R., Bracegirdle, T. J., Dutrieux, P., Jenkins, A., & Steig, E. J. (2019). West Antarctic ice loss influenced by internal climate variability and anthropogenic forcing. *Nature Geoscience*, 1–7.

Hoyer, S., & Hamman, J. (2017). xarray: N-D labeled arrays and datasets in

Python. *J. Open Res. Softw.*, *5*(1). Retrieved from `https://doi.org/10.5334/jors.148` doi: 10.5334/jors.148

Hunter, J. D. (2007). Matplotlib: A 2D graphics environment. *Computing in Science & Engineering*, *9*(3), 90–95. doi: 10.1109/MCSE.2007.55

Huot, P.-V., Kittel, C., Fichefet, T., Jourdain, N. C., Sterlin, J., & Fettweis, X. (2021). Effects of the atmospheric forcing resolution on simulated sea ice and polynyas off Adélie Land, East Antarctica. *Ocean Modelling*, *168*, 101901.

Jenkins, A., Shoosmith, D., Dutrieux, P., Jacobs, S., Kim, T. W., Lee, S. H., ... Stammerjohn, S. (2018). West Antarctic Ice Sheet retreat in the Amundsen Sea driven by decadal oceanic variability. *Nature Geosc.*, *11*, 733–738.

Jourdain, N. C., Asay-Davis, X., Hattermann, T., Straneo, F., Seroussi, H., Little, C. M., & Nowicki, S. (2020). A protocol for calculating basal melt rates in the ISMIP6 Antarctic ice sheet projections. *The Cryosphere*, *14*(9), 3111–3134.

Jourdain, N. C., Mathiot, P., Merino, N., Durand, G., Le Sommer, J., Spence, P., ... Madec, G. (2017). Ocean circulation and sea-ice thinning induced by melting ice shelves in the Amundsen Sea. *J. Geophys. Res. Oceans*, *122*(3), 2550–2573.

Jourdain, N. C., Merino, N., Le Sommer, J., Durand, G., & Mathiot, P. (n.d.). *Interannual iceberg meltwater fluxes over the Southern Ocean (1.0)* (Tech. Rep.).

Knutti, R., Furrer, R., Tebaldi, C., Cermak, J., & Meehl, G. A. (2010). Challenges in combining projections from multiple climate models. *J. Climate*, *23*(10), 2739–2758.

Krinner, G., & Flanner, M. G. (2018). Striking stationarity of large-scale climate model bias patterns under strong climate change. *Proceedings of the National Academy of Sciences*, *115*(38), 9462–9466.

Levermann, A., Winkelmann, R., Albrecht, T., Goelzer, H., Golledge, N. R., Greve, R., ... others (2020). Projecting Antarctica's contribution to future sea level rise from basal ice shelf melt using linear response functions of 16 ice sheet models (LARMIP-2). *Earth System Dynamics*, *11*(1), 35–76.

Madec, G., & NEMO-team. (2016). *NEMO ocean engine, version 3.6 stable, Note du Pôle de modélisation de l'Institut Pierre-Simon Laplace No 27, ISSN No 1288-1619* (Tech. Rep.). IPSL, France.

Mathiot, P., Jenkins, A., Harris, C., & Madec, G. (2017). Explicit and parametrised representation of under ice shelf seas in az* coordinate ocean model NEMO 3.6. *Geosci. Model Dev.*, *10*(7), 2849–2874.

Merino, N., Jourdain, N. C., Le Sommer, J., Goosse, H., Mathiot, P., & Durand, G. (2018). Impact of increasing antarctic glacial freshwater release on regional sea-ice cover in the Southern Ocean. *Ocean Model.*, *121*, 76–89.

Merino, N., Le Sommer, J., Durand, G., Jourdain, N. C., Madec, G., Mathiot, P., & Tournadre, J. (2016). Antarctic icebergs melt over the Southern Ocean : climatology and impact on sea-ice. *Ocean Model.*, *104*, 99–110.

Morlighem, M. (2020). *MEaSUREs BedMachine Antarctica, Version 2* (Tech. Rep.). Boulder, Colorado USA. NASA National Snow and Ice Data Center Distributed Active Archive Center. Retrieved from `https://nsidc.org/data/NSIDC-0756/versions/2` doi: 10.5067/E1QL9HFQ7A8M

Morlighem, M., Rignot, E., Binder, T., Blankenship, D., Drews, R., Eagles, G., ... others (2020). Deep glacial troughs and stabilizing ridges unveiled beneath the margins of the Antarctic ice sheet. *Nature Geoscience*, *13*(2), 132–137.

Nakayama, Y., Menemenlis, D., Zhang, H., Schodlok, M., & Rignot, E. (2018). Origin of Circumpolar Deep Water intruding onto the Amundsen and Bellingshausen Sea continental shelves. *Nat. Comm.*, *9*(1), 1–9.

Nakayama, Y., Timmermann, R., Schröder, M., & Hellmer, H. H. (2014). On the difficulty of modeling Circumpolar Deep Water intrusions onto the Amundsen Sea continental shelf. *Ocean Model.*, *84*, 26–34.

Naughten, K. A., Holland, P. R., Dutrieux, P., Kimura, S., Bett, D. T., & Jenkins,

A. (2022). Simulated twentieth-century ocean warming in the Amundsen Sea, West Antarctica. *Geophys. Res. Lett.*, e2021GL094566.

Naughten, K. A., Meissner, K. J., Galton-Fenzi, B. K., England, M. H., Timmermann, R., & Hellmer, H. H. (2018). Future projections of Antarctic ice shelf melting based on CMIP5 scenarios. *J. Climate*, *31*(13), 5243–5261.

Nowicki, S., Payne, A., Goelzer, H., Seroussi, H., Lipscomb, W., Abe-Ouchi, A., ... van de Wal, R. (2020). Experimental protocol for sea level projections from ISMIP6 standalone ice sheet models. *The Cryosphere*, *14*, 2331–2368. doi: 10.5194/tc-14-2331-2020

Purich, A., & England, M. H. (2021). Historical and future projected warming of Antarctic Shelf Bottom Water in CMIP6 models. *Geophys. Res. Lett.*, *48*(10), e2021GL092752.

Rousset, C., Vancoppenolle, M., Madec, G., Fichefet, T., Flavoni, S., Barthélemy, A., ... others (2015). The Louvain-La-Neuve sea ice model LIM3.6: global and regional capabilities. *Geosci. Model Dev.*, *8*(10), 2991–3005.

Seroussi, H., Nowicki, S., Payne, A. J., Goelzer, H., Lipscomb, W. H., Abe-Ouchi, A., ... others (2020). ISMIP6 Antarctica: a multi-model ensemble of the Antarctic ice sheet evolution over the 21st century. *The Cryosphere*, *14*(9), 3033–3070.

Siahaan, A., Smith, R., Holland, P., Jenkins, A., Gregory, J. M., Lee, V., ... Jones, C. (2021). The Antarctic contribution to 21st century sea-level rise predicted by the UK Earth System Model with an interactive ice sheet. *The Cryosphere Discussions*, 1–42.

Smith, R. S., Mathiot, P., Siahaan, A., Lee, V., Cornford, S. L., Gregory, J. M., ... others (2021). Coupling the UK Earth System Model to dynamic models of the Greenland and Antarctic ice sheets. *J. Adv. Model. Ea. Sys.*, *13*(10), e2021MS002520.

Spence, P., Griffies, S. M., England, M. H., Hogg, A. M., Saenko, O. A., & Jourdain, N. C. (2014). Rapid subsurface warming and circulation changes of Antarctic coastal waters by poleward shifting winds. *Geophys. Res. Lett.*, *41*(13), 4601–4610.

Swart, N. C., & Fyfe, J. C. (2012). Observed and simulated changes in the Southern Hemisphere surface westerly wind-stress. *Geophys. Res. Lett.*, *39*(16).

Timmermann, R., & Hellmer, H. H. (2013). Southern Ocean warming and increased ice shelf basal melting in the twenty-first and twenty-second centuries based on coupled ice-ocean finite-element modelling. *Ocean Dyn.*, *63*(9-10), 1011–1026.

Williamson, D. B., Blaker, A. T., & Sinha, B. (2017). Tuning without over-tuning: parametric uncertainty quantification for the NEMO ocean model. *Geosci. Model Dev.*, *10*(4), 1789–1816.